4-15-2013

Detecting Geyser Activity with Infrasound

Jeffrey B. Johnson
Boise State University

J. F. Anderson
New Mexico Tech

R. E. Anthony
New Mexico Tech

M. Sciotto
Università di Catania

Detecting Geyser Activity with Infrasound

J. B. Johnson
Boise State University

J. F. Anderson
New Mexico Tech

R. E. Anthony
New Mexico Tech

M. Sciotto
Università di Catania

Abstract

We monitored geyser activity in the Lower Geyser Basin (LGB) of Yellowstone National Park with dual four-element microphone arrays separated by ~600 m. The arrays were independently used to identify incident coherent plane wave energy, then conjoint cross beam back-azimuths from the two arrays were used to precisely locate signal sources. During a week in August 2011 we located repeating infrasound events, peaked in energy between 1 and 10 Hz, originating from at least five independent geothermal features, including the episodically erupting Great Fountain, Fountain and Kaleidoscope Geysers, as well as periodic infrasound from nearby Botryoidal and persistent sound from Firehole Spring. Although activity from nearby cone-type geysers was not detected in the infrasound band up through 50 Hz, the major fountain-type geysers (i.e., with columns greater than 10 m) could be detected at several kilometers, and two minor geysers (i.e., a few meters in eruption height) could be tracked at distances up to a few hundred meters. Detection of geyser activity was especially comprehensive at night when ambient noise was low. We conclude that infrasound monitoring of fountain-type geysers permits convenient tracking of geyser activity, episodicity, signal duration, energy content, and spectral content. These parameters enable objective statistical quantification of geyser behavior and changes over time that may be due to external forcing. Infrasonic study of geyser activity in an individual basin has great monitoring utility and can be reasonably accomplished with two or more distributed sensor arrays.

Keywords: geyser; Yellowstone; infrasound monitoring; array analysis

1.0 Introduction

Geyser sound and volcano sound generation may be considered analogous in a number of respects. In both systems, volatiles can reach a liquid's free surface (water in the case of the geyser; silicate melt in the case of the volcano) and burst with considerable overpressure relative to the atmosphere. In volcanic systems both the distension of the free surface due to sub-surface strains [**Garces & McNutt, 1997; Yokoo & Iguchi, 2010**], and the expansion of gas following fragmentation [**Ripepe & Gordeev, 1999; Jones et al., 2008**], have been considered as volumetric sources, which produce intense low-frequency sounds. High-velocity emissions of gas and/or condensed phases are also responsible for jetting sounds at volcanoes [**Woulff & McGetchin, 1976; Matoza et al., 2009**], which may serve as analogues for certain geysers that erupt as collimated jets of water and steam.

The style and vigor of a volcanic eruption generally dictates the spectral content and intensity of the radiated sound. For relatively low-energy explosive volcanic eruptions, often characterized as strombolian or vulcanian, the radiated sound is most intense around the near-infrasound band (and specifically in the frequency range of a few seconds to a few Hz) [**Marchetti et al., 2009; Johnson et al., 2004**]. These low frequencies predominate because of the relatively large physical dimension and long duration of source movements, such as bubble oscillations or gas expansion [**Vergniolle & Brandeis, 1996; Gerst et al., in rev.**]. Geysers, though smaller in physical scale than volcanoes, are still capable of producing relatively large volume fluid ejections with columns as wide as a few meters and as high as a few tens of meters. Accordingly, fountain-type geysers radiate predominantly low frequency acoustic energy in the near-infrasound band (1-20 Hz).

Geophysical sources of infrasound, including volcanoes, earthquakes, avalanches, thunder, bolides, and storms, are amenable to remote monitoring and tracking in large part because infrasonic frequencies attenuate slowly with distance [**Arrowsmith et al., 2010**]; however, geophysical infrasound detection and interpretation is often obscured by unwanted signals (e.g., human activity or microbaroms) or noise contributions from atmospheric winds [**Bowman et al., 2005; Fee & Garces, 2007**]. In order to distinguish targeted signals from noise microphone arrays are typically deployed to identify signal coherency and source direction [**Rost & Thomas, 2002**]. Toward the goal of locating and tracking geyser activity at Yellowstone, we deployed two separated infrasound microphone arrays in August of 2011.

Although various seismic surveys have been carried out at geysers to study ground-propagating elastic waves [e.g., **Kieffer, 1984**; **Kedar et al., 1996**] this work is the first of its kind to investigate broadband sound waves radiated from geysers into the atmosphere.

2.0 Background

Yellowstone National Park in Wyoming, USA hosts the world's densest concentration of geysers with about 500 active in a typical year, or more than half the world's total. Most of Yellowstone's geysers are located in three basins, Upper Geyser Basin (UGB), Lower Geyser Basin (LGB), and Norris Basin, which are extensive geographic regions that comprise distinct groups of thermal features. For instance, the LGB, which is the focus of this study, is 13 km^2 in area and has more than 1500 thermal features organized into about 13 distinct groups [**Bryan, 2008**]. Classification as a geyser requires that a thermal feature exhibit intermittent discharge of water accompanied by steam. According to **Bryan et al. (2008)** there are well over one hundred features that qualify as geysers in the LGB alone.

Because we anticipated that violent ejection of steam and water is most likely to generate high signal-to-noise infrasound we deployed our microphone arrays within a few hundred meters of Great Fountain, one the most prominent geysers of the LGB. Though Great Fountain Geyser is located near the eastern edge of the LGB, we still anticipated recording geyser activity from other nearby features. Table 1 provides a list of some of the LGB geysers, where plume height in excess of a few meters is often reported [e.g., **Bryan et al., 2008**]. A map showing these geysers and our microphone arrays is provided in Figure 1. Despite having fewer major geysers than the UGB, the LGB provided an excellent test bed for acoustic monitoring because of lower tourist traffic and associated cultural noise.

Table 1 callout

Figure 1 callout

3.0 Experiment

We deployed two four-element infrasound arrays in the LGB between Aug. 8th (Julian Day 220) and Aug. 14th (Julian Day 226) of 2011. These arrays consisted of four identical low-frequency microphones with flat response between 0.02 Hz and a Nyquist frequency of 50 Hz. Linear dynamic range of the instruments was +/-125 Pa and noise floor in the 1 to 10 Hz band was ~2 mPa rms [**Marcillo et al., 2012**]. Three of the array elements were positioned at the vertices of an approximate equilateral triangle and connected to the central datalogger by 30-m cables. A fourth microphone was co-located at the center of the array next to a 6-channel, 24-bit logger (Refraction Technology RT-130) recording continuously at 100 Hz. GPS timing of the loggers allowed coordination between the two arrays, and kinematic GPS surveying provided sensor node locations accurate to within ~0.5 m in the horizontal and ~1 m in the vertical.

The array centers were separated from each other by 620 m. The midpoint of the two arrays, or network center, was located at 110.802° W, 44.537° N, and 2237 m above sea level, and is used as the coordinate reference for mapped acoustic sources. The purpose of dual arrays was to identify and locate sources producing coherent signals. We identify source locations by first using each four-element array to independently determine back-azimuth of coherent infrasound. Then we find the intersection region of the back-azimuth beams to identify the responsible geyser. Owing to the distribution of the two arrays, location resolution and errors are azimuthally and radially variable. We discuss location uncertainties as part of our study's 'network response'. The 'array response', a function of array geometry, is also examined as it influences aliasing and back-azimuth uncertainty.

3.1 Array Response and Precision

The array response of a distribution of sensors characterizes the susceptibility of an array to aliasing. Such aliasing is problematic for arrays with apertures that are large relative to incident plane wave wavelengths and is especially pronounced in four-element arrays with equal spacing between sensor nodes [**Christie and Campus, 2010**]. The normalized theoretical wavenumber response of an *n*-element array is a function of 2-D wavenumber (k_x and k_y) [**Rost & Thomas, 2002**]:

$$R(k_x,k_y)=\frac{1}{n^2}\left|\sum_{i=1}^{n} e^{-\sqrt{-1}\left(k_x x_i+k_y y_i\right)}\right|^2 \qquad \textbf{Eqn. 1}$$

The array output is the convolution of the array response and the horizontal wavefield defined by a propagation vector. An ideal array response has a single peak at the origin (k_x=0 and k_y=0) and negligible side lobe peaks.

Array responses with significant sidelobes (see Figures 2b,e for the West and East arrays respectively) are susceptible to possible aliasing. To illustrate the potential ambiguity associated with ~5 Hz infrasound tone suppose that a recording on channel #1 of the West Array exhibits a phase shift of half a cycle relative to channels #2-4. In the absence of other information these observations could be attributed either to horizontally propagating acoustic energy coming from either the WNW or the ESE, corresponding to two different array response peaks. For our local geyser sources we assume propagation must be sub-horizontal (i.e., $f=(c/2\pi)\sqrt{k_x^2+k_y^2}$; Figure 2). This, coupled with the facts that geyser infrasound is generally broadband (with frequencies less than 5 Hz) and often has transient pulses, limits our arrays' susceptibility to aliasing.

Array back-azimuth precision is limited by small array dimension and/or coarse timing resolution for correlated phases crossing the array elements. For our digital data the precision of cross-correlation lag

times is discretized to the nearest sample, which is 0.01 s in our analysis. Subsequent back-azimuth determination (see source localization section below) is calculated by inverting these rounded phase lag times. To anticipate the associated error due to time discretization we calculate time of arrivals for incident rays crossing the arrays at a range of azimuths and then round these arrival times to the nearest 0.01 s before inverting for an inferred back-azimuth. For 360 different plane waves crossing the arrays at 1° azimuthal increments the standard deviation difference between actual and calculated azimuths are 1.9 and 1.6 degrees for the West and East arrays respectively (Figure 2c,f).

Figure 2 Callout

3.2 Network Response

Our two arrays separated by 620 m are used to locate infrasound sources when source back-azimuths cross obliquely. The compass azimuth (relative to true North, or 0°) connects the West array to the East array at 87° and the azimuth connecting East to West array is -93° (or 267°). As such, back-azimuth beams cross for

$$\theta_W > \theta_E \text{ when } -93 < \theta_W < 87 \text{ and } -93 < \theta_E < 87$$

or **Eqn. 2**

$$\theta_W < \theta_E \text{ when } 87 < \theta_W < 267 \text{ and } 87 < \theta_E < 267$$

where θ_W and θ_E are the compass bearing back-azimuths from the West and East arrays to the source. Overlapping back-azimuth directions are indicated as colored regions in Figure 3, which also show the corresponding distance and azimuth to the crossing beams (Figures 3a,b). These parameters are determined by computing the locations of converging beams (i.e., the inferred source location) for all possible permutations of θ_W and θ_E (ranging from -93 to 267°).

Figure 3 Callout

Errors in source location distance (Figure 3c) are calculated as the magnitude of the gradient of Figure 3a. At a distance *r* the distance error per degree of back-azimuth uncertainty is defined as:

$$e_r = \sqrt{\left(\frac{\partial r}{\partial \theta_W}\right)^2 + \left(\frac{\partial r}{\partial \theta_E}\right)^2} \qquad \textbf{Eqn. 3}$$

For instance, the 100-m/° contour in Figure 3c implies that the distance to a source (e.g., the Fountain Group (FG)) is uncertain to ~100 m for a back-azimuth uncertainty of one degree. An azimuthal error (Figure 3d) is transverse to the radial error and is computed from the azimuth to the source (Figure 3b) as:

$$e_\theta = r\sqrt{\left(\frac{\partial \theta}{\partial \theta_W}\right)^2 + \left(\frac{\partial \theta}{\partial \theta_E}\right)^2} \qquad \textbf{Eqn. 4}$$

Generally, radial uncertainties are much larger than azimuthal uncertainties and both uncertainties increase for greater source-receiver distances.

4.0 Source localization

Our procedure to locate robust infrasound sources using dual arrays involves identification of coherent energy arriving coincidentally at both arrays. Coherency at a single array is established if timing of phase lags, determined through cross-correlation of the array elements, is internally consistent. If so, potential source back-azimuths may be calculated. For coherent energy that traverses both arrays simultaneously a candidate source is mapped as the intersection of two back-azimuths. This potential source is reliable if its position is in agreement with the phase delay observed between beam-stacked waveforms at the WA and EA.

4.1 Back-azimuth determination

Phase lags between two elements of a microphone array are determined through cross-correlation of pairs of sensors. For *m* elements in an array there are $\sum_{i=1}^{m-1} i$ unique sensor pair combinations that can be cross-correlated. For a cross-correlation to be considered significant it must exceed a normalized cross-correlation threshold, which we fix in this study at the 95% confidence level for cross-correlated white noise. For *n* samples $2/\sqrt{n}$ is the expected normalized cross-correlation for Gaussian white noise. For our 4 node arrays and 20 s (2000 sample) comparison windows a normalized cross-correlation threshold of 0.045 must be exceeded on all 6 station pairs. More stringent cross correlation thresholds should probably be applied for three element arrays, which have only 2 unique station pair comparisons.

In addition to correlation threshold, strict consistency criteria must be met. Lag times of peak cross-correlation are calculated for sliding windows and checked for internal consistency similar to that used in the PMCC technique [**Cansi, 1995]**. While **Cansi (1995)** searches for consistency amongst unique triad pairs, our processing requires consistency amongst all unique quad pairs. For our four-element array there are 3 unique sequences of quad pair comparisons: ch1↔ch2↔ch3↔ch4↔ch1, ch1↔ch3↔ch2↔ch4↔ch1, and ch1↔ch2↔ch4↔ch3↔ch1. Internal consistency is met when the summed phase lags of the quad pairs sum toward zero, i.e. $\left|\varepsilon_{ijkl} t_{ij} + \varepsilon_{ijkl} t_{jk} + \varepsilon_{ijkl} t_{kl} + \varepsilon_{ijkl} t_{li}\right| \le \chi$. Here the indices *i,j,k,* and *l* refer to one of the 4 sensor array channels. The variable t_{ij} is the lag time associated with peak waveform cross-correlation and ε_{ijkl} is the Levi-Civita symbol, where only non-repeating index permutations are non-zero, +1 or -1, and sign is dependent upon the order of indices. Because of digital signal discretization, which rounds correlation phase lags to the nearest sample, we require the absolute value of consistency to be less than or equal to χ=4 samples.

Consistent phase lags for unique quad sequences are used to compute a back-azimuth by inverting for the horizontal projection of the slowness vector $\vec{s} = \{s_x, s_y\}$. Following the inversion procedure outlined in **Arechiga et al. (2011)** time lags are related to the slowness vector by

$$\begin{bmatrix} t_{ij} \\ t_{jk} \\ t_{kl} \\ t_{li} \end{bmatrix} = \begin{bmatrix} dx_{ij} & dy_{ij} \\ dx_{jk} & dy_{jk} \\ dx_{kl} & dy_{kl} \\ dx_{li} & dx_{li} \end{bmatrix} \begin{bmatrix} s_x \\ s_y \end{bmatrix} \qquad \textbf{Eqn. 5}$$

where *dx* and *dy* are the GPS surveyed east-west and north-south separation distances between pairs of sensor elements in an individual array. The distance matrix, denoted as *D*, can be represented as a two-column matrix because the vertical separation distance is assumed zero (i.e., $dz_{ij} = dz_{jk} = dz_{kl} = dz_{li} = 0$) as all sensor nodes were deployed on an approximately level surface to within ~1 m precision.

Because the solution to the slowness vector for $t = Ds$ is overdetermined we solve it using a least squares solution with the generalized inverse of *D*, where $D^{-g} = \left(D^T D\right)^{-1} D^T$ and the slowness vector is solved as $s = D^{-g} t$. A third (vertical) component of the slowness vector can be computed assuming that the coherent arrival is an acoustic plane wave with speed *c*, where $s_z = \sqrt{c^{-2} - s_x^2 - s_y^2}$.

Imaginary values of s_z imply impossibly low slowness values for acoustic waves traversing the array, however near-horizontal acoustic waves may potentially result in imaginary vertical slowness values due to cross-correlation timing discretization, which leads to rounded values of *t* and values of s_x and s_y, which may be rounded upwards. For this reason we consider that horizontal slownesses, which exceed the slowness amplitude (c^{-1}) by less than 10%, may be treated as horizontally propagating acoustic waves with zero degree elevation angles (i.e., $s_z=0$). We use the following conventions to calculate vertical slowness:

$$\begin{aligned} s_z &= imaginary \quad \text{for} \quad c^{-1} < 0.9 \times \sqrt{s_x^2 + s_y^2} \\ s_z &= 0 \quad \text{for} \quad 0.9 \times \sqrt{s_x^2 + s_y^2} \le c^{-1} \le \sqrt{s_x^2 + s_y^2} \\ s_z &= \sqrt{c^{-2} - s_x^2 - s_y^2} \quad \text{for} \quad \sqrt{s_x^2 + s_y^2} < c^{-1} \end{aligned} \qquad \textbf{Eqn. 6}$$

When s_z is imaginary we consider the arrival to be spurious.

From the acoustic wave slowness vector the back-azimuth and incidence are determined. Azimuth of the plane wave is calculated using the trigonometric relations:

$$\begin{aligned} \theta &= \arctan\left(s_x / s_y\right) \quad \text{for} \quad s_y > 0 \\ \theta &= \arctan\left(s_x / s_y\right) + 180° \quad \text{for} \quad s_y < 0 \end{aligned} \qquad \textbf{Eqn. 7}$$

while plane wave elevation angle, as measured from the horizontal, is

$$\phi = \arcsin\left(c\, s_z\right) \qquad \textbf{Eqn. 8}$$

In this analysis of local geyser sources in the LGB propagation is expected to be sub-horizontal. Thus, we ignore signals with values of ϕ greater than 15°. We note that more steeply incident acoustic energy observed during our study is often moving and attributable to aircraft.

Back-azimuths for internally consistent array detections are independently calculated for the three unique permutations of sensor pair correlations, i.e. $ijkl = \{1234, 1243, 1324\}$ and then averaged. These back-azimuths may then be plotted as a function of time to show the temporal evolution of potential acoustic source directions. The example of Figure 4 shows a one-hour period (starting August 10th at 10:00 PM local time) when three distinct geyser sources were detected.

Callout Figure 4

4.2 Cross beam source localization and validation

Together the back-azimuths from the West and East arrays are used to locate potential geyser sources. Back-azimuth beams from the two arrays converge under the conditions specified in **Eqn. 2**. Cross beam intersection then occurs at a location x_0, y_0 where

$$x_0 = x_W + \sin\theta_W \left[\frac{(y_W - y_E)\sin\theta_E - (x_W - x_E)\cos\theta_E}{\sin\theta_W \cos\theta_E - \cos\theta_W \sin\theta_E} \right]$$

and **Eqn. 9**

$$y_0 = y_W + \cos\theta_W \left[\frac{(y_W - y_E)\sin\theta_E - (x_W - x_E)\cos\theta_E}{\sin\theta_W \cos\theta_E - \cos\theta_W \sin\theta_E} \right]$$

Here x_W, y_W and x_E, y_E correspond to the UTM coordinates of the West and East arrays respectively.

A candidate source location is identified for converging beams when coherent energy is conjointly identified on both arrays (i.e., during the same 20 s sliding window period). In this case beam waveform stacks (see **Eqn. 10** below) are produced for each array and a cross-correlation time lag is calculated for the two beams. These inter-network lag times indicate potential source locations lying along hyperbolic curves (Figure 5). If the hyperbolic curve for a given lag time coincides with the cross-beam intersection locus x_0, y_0 then we consider that source location to be robust.

Callout Figure 5

Source locations are plotted with footprints that scale with back-azimuth uncertainty. An azimuthal uncertainty for each array is determined as the 95% confidence intervals for estimated errors (3.6° for West Array and 2.5° for East Array; Figures 2e,f). Error ellipses in Figure 5 are centered on the intersection of back-azimuths and have axes with dimensions of angular and radial uncertainties. It is evident that location uncertainty increases markedly for more distant sources as predicted by the network response (Figure 3). For instance, for the Fountain Geyser source, radial distance error is as great as half a kilometer. Locations of geysers and other infrasound sources are shown in an animation that is provided as auxiliary materials. This movie shows a 5-day sequence of mapped sources, in the form of Figure 5, for hourly time increments.

5. Results

5.1 Interpretation of beam stacks

Reliable source locations can be used to produce array beam stacks $dp_b(t)$, which provide improved signal-to-noise over waveforms from individual channels. To create a beam stack the excess pressure waveforms in an individual array $dp_i(t)$ are shifted by retardation times corresponding to relative locations and incident slowness vector and then stacked (Figure 6):

$$dp_b(t) = \frac{1}{m} \sum_{i=1}^{m} dp_i\left(t + dx_{ij} s_x + dy_{ij} s_y\right) \qquad \textbf{Eqn. 10}$$

In our study we calculate a center node beam array stack where *j* is channel 1.

Similarity between the beam stack waveforms of the two arrays is variable and depends upon signal strength, background noise, and frequency band. For the four time windows displayed in Figure 6 the signal correlation is indicated for both broadband infrasound and four narrow-band overlapping frequencies. Signal similarity and relative delay times are quantified from the peak normalized cross-correlation of band-passed waveforms. Higher signal-to-noise waveforms, such as the ones displayed in Figure 6a-b, are more highly correlated than smaller transients, such as those shown in Figure 6c-d.

Figure 6 Callout

For the featured data in Figure 6 cross-network correlation is generally greatest in near-infrasound and low audio band (1-32 Hz) although this varies somewhat depending upon the particular source. For example, Figure 6a corresponds to infrasound originating from the Northeast and external to the LGB. For this event peak signal correlation between arrays occurs in the band 0.25 to 2 Hz and candidate source types could include earthquakes, bolides, thunder, or cultural signal (such as aircraft or explosions) [**Arrowsmith et al., 2010**]. In this particular case, we feel the most probable signal source is distant thunder owing to the signal shape and amplitude, intermittency (many events from this direction occurring over tens of minutes), and spectral content similar to that previously observed for thunder [e.g., **Assink et al., 2008**; **Arechiga et al., 2011**].

Geyser sources including Fountain Geyser (Figure 6b), Botryoidal Spring (Figure 6c), and Firehole Spring (Figure 6d) are also identified during the hour starting at 10:00 PM local time on August 10th. Fountain Geyser and Botryoidal Spring signal correlation is greatest in the 0.25-2 Hz bands while Firehole Spring is best identified in the 1-8 Hz band. Correlation lag times are consistent with sources at Fountain Geyser, Botryoidal Spring, and Firehole Spring and corroborate cross beam locations of the geyser sound sources. Notably, the low-amplitude correlated signal from both Firehole and Botryoidal Spring is not clearly evident through visible inspection of the time series data. For these geysers relatively high levels of ambient infrasound noise are indicated by similarities between the spectra for the events and pre-event noise windows (Figure 8c, f). Filtering above ~0.25 Hz coupled with array and/or network analysis is thus vital to identify and track activity from 'quieter' geysers.

5.2 Geyser detection

Dual array cross beaming and validation through inter-array lag time delays enable robust identification of geyser and/or other signals. If the source coincides with a known geyser feature, e.g. referenced in **Bryan (2008)**, we consider it to be a geyser signal. During the week-long monitoring interval in August 2011 we identified at least five repeating geyser sources and potential activity from several others. In general, geyser detection was affected by levels of wind, which contribute to ambient noise throughout the near infrasound band. Obfuscation of geyser signal in the LGB was particularly pronounced during windy afternoons, however nighttime recordings had much improved signal-to-noise (refer to summary of 5-day record in Figure 7). The five primary identified LGB sources were Great Fountain (130 m), Firehole Spring (165 m), Botryoidal Spring (265 m), Fountain Geyser (1706 m), and at least one source from Kaleidoscope Group (2171 m). Descriptions of their activity, including episodicity and eruption duration, are given below.

Figure 7 Callout

5.2.1 Great Fountain

Ten eruptions of Great Fountain were detected during the 5-day study interval shown in Figure 7. Activity of main events is separated by 11 to 19 hour intervals and duration of detected events ranges from 45 to 75 minutes with one event lasting 130 minutes. This long-duration event precedes an exceptionally long 19-hour quiescent interval suggesting that more voluminous eruptions may require longer recharge intervals. Great Fountain infrasound records corroborate anecdotal observations that most events are composed of 4 or more pulses of 5 to 20 minute duration separated by up to 15 minutes of quiet (Figure 7). A detailed

example of a typical event from Great Fountain, along with its normalized power spectrum, is provided in Figure 8a.

Figure 8 Callout

Characteristic event durations and intervals between events can easily be quantified from the overview records of Figures 7 and 9a, which both show detections as a function of time. For our 5-day monitoring interval the eruption durations *D* appear correlated with inter-eruption intervals *I*, i.e. $I = 4.9 \times D + 7.1$ hours (*r-squared* value of 0.73). Despite our short observation period these observations exhibit similarities with previous eyewitness observations cited in **Bryan (2008)** where $I = 7 \times D + 6$ hours (Figure 9b).

Figure 9 Callout

Due to the relative intensity of the Great Fountain infrasound source and its proximity to both infrasound arrays the signal from this geyser is often identifiable through visual inspection of the time series after filtering above the microbarom band. Peak-to-peak amplitude of the largest pulses from a Great Fountain sequence occasionally exceed 2 Pa recorded at the East Array (276 m distant). These peak-amplitude pulses are bipolar ~2 Hz wavelets, with asymmetrically larger compression than rarefaction. They accompany explosive bursts from the geyser's vent, which manifest voluminous vapor and water columns reaching 30 to 50 m high. Smaller explosive bursts, as seen in video records, are correlated with less intense infrasound pulses. Impulsivity, frequency content, and bimodal pulse shape are reminiscent of explosion infrasound N-wave signals accompanying explosions of pressurized gas at many erupting volcanoes [**Johnson & Ripepe, 2011**].

Band-limited acoustic power radiated from a monopole into a homogeneous hemisphere may be quantified from filtered infrasound recordings according to **Dowling (1998)**:

$$P(t) = \frac{2\pi r^2}{\rho c} \int_{t}^{t+\Delta t} \frac{\delta p^2\left(\tau + r/c\right)}{\Delta t} d\tau \qquad \textbf{Eqn. 11}$$

where Δt is the averaging interval over which power is calculated, set here at 1 s, and r is the atmospheric density, approximated as 1.0 kg/m^3. Cumulative energy can then be calculated as the time integrated acoustic power:

$$E(t) = \frac{2\pi r^2}{\rho c} \int_0^t \delta p^2 \, (\tau + r/c) d\tau \qquad \textbf{Eqn. 12}$$

For the most intense Great Fountain pulses, power can exceed 300 Watts averaged over a 1-s interval (Figure 8a). Cumulative energy over the course of an hour-long event (t = 3600 s) is several thousand Joules, or slightly less than 1 Watt averaged over a Great Fountain event.

For some Great Fountain events the infrasound network identifies potential short (minute-long) precursors occurring an hour to several hours prior to the main eruption. Geyser observers at Great Fountain have commonly reported this activity as 'pre-play' that accompanies boiling and overflow from the vent occurring on average 85 minutes prior to the main event [**Bryan et al., 2008**]. Of the ten events detected in our infrasound records half of them show these precursory infrasound signals occurring prior to the main event (see indicated red arrows in Figure 9a). Infrasound monitoring has the potential to identify pre-play and quantify how long and how often it precedes Great Fountain eruptions. As with statistics relating event duration and quiescent intervals we suggest that longer monitoring periods will facilitate robust statistical relationships.

5.2.2 Fountain Geyser and Kaleidoscope Group

Fountain Geyser, not to be confused with Great Fountain, is the major geyser of the regularly performing features in the Fountain Group, located about 1700 m from the center of our twin infrasound arrays. During nighttime periods of relative low wind and quiet (9:00 PM through 10:00 AM) events from Fountain were routinely recorded. During our five-day observation period 13 events were identified and 11 probable events were missed due most likely to ambient wind noise. Non-detected events were inferred from the exceptional regularity of Fountain Geyser eruptions.

From our infrasound records we detect eruptions with regular intervals of 5.9 +/- 0.3 hours that appear to correlate with 'long mode intervals' discussed by **Bryan (2008)** for Fountain Geyser. Infrasonic waveforms from Fountain Geyser events were also remarkably similar, beginning and terminating abruptly, with detections lasting between 27 and 36 minutes (for 11 events). Signal envelope was substantially different from that of Great Fountain with less intense pulses, but more sustained amplitude reminiscent of a stationary volcanic broadband tremor (Figure 8b). At the distance of the East Array peak-to-peak tremor amplitudes occasionally exceeded 0.1 Pa, which would reduce to ~1 Pa at 100 m invoking a $1/r$ pressure decay for a homogeneous atmosphere. The nature of the infrasound is suggestive of the descriptions of typical Fountain activity, which reportedly begins abruptly and then plays in a sustained fashion with splashing and a wide column up to 15 m in height [**Bryan et al., 2008**]. Cumulative infrasound power radiated from Fountain totals several thousand Joules and is comparable to infrasound from Great Fountain events.

Sporadic infrasound originating from the vicinity of Fountain Group, but with a slightly more westerly back-azimuth (335°), was intermittently recorded during our week-long survey. Although this back-azimuth is close to that of Fountain Geyser (342°) the location ellipsoids from this source are spatially distinct from Fountain Geyser and we conclude that they represent a separate source occurring at slightly greater distant range (~2000 m) than the Fountain Group (~1700 m). We speculate this is Kaleidoscope Group geyser activity that is characterized by infrasound with a few bursts that last just a few minutes (e.g., on Julian Day 223 at 07:20 UTC). Based upon the infrasound character the most likely candidate geyser source is the namesake Kaleidoscope Geyser, which hosts short-duration activity (20 to 120 s) that suddenly shoots water jets 15 to 35 m [**Bryan et al., 2008**].

5.2.3 Botryoidal and Firehole Springs

Infrasound radiation from Botryoidal Spring is routinely identified during periods of low background noise, i.e. when other 'louder' geysers are quiet and when wind-induced noise is low. During these conditions the activity from Botryoidal, which is 338 m from the East Array, is periodic. During our observational period infrasound bursts occurred with remarkable regularity at intervals of 4.5 +/- 0.5 minutes (Figures 8c and 10). Interval times between successive event detections are consistent with a normal distribution (Figure 10).

Figure 10 Callout

Transient signal amplitudes from Botryoidal are invariably small and short in duration, typically only 0.05 Pa and composed of only one or a couple of 2.5 Hz oscillations. This spectral content is somewhat higher than the peak acoustic frequencies of the larger Great Fountain and Fountain Geysers, which were both peaked in the 0.5 to 1.5 Hz band (Figure 8a, b). In general the infrasound observations of Botryoidal are consistent with anecdotal reports. In recent years reported periodicity has ranged between 2.5 and 5.5 minutes. Eruptions consist of single steam bubbles distending the surface of the spring before bursting and throwing water to heights of 4 to 6 m [**Bryan et al., 2008**].

Nearby Firehole Spring is another geothermal feature, which produces prodigious (but even lower-amplitude) infrasound. Owing to its near-continuous activity Firehole Spring is sometimes considered a 'perpetual spouter' with play typically reaching only a few meters in height [**Bryan, 2008**]. Its corresponding infrasound is manifested as a persistent infrasonic tremor of such low intensity that it is generally not detected except during the most quiet of intervals, when it is registered as a quasi-continuous source. At a source-receiver distances of ~350 m Firehole Spring infrasound is not visually apparent in time series records and it is at the limits of signal detection using array analysis techniques. The spectral content of Firehole Spring activity is peaked notably higher (>4 Hz) than the other frequently detected geysers.

6.0 Discussion

We recorded infrasound radiation associated with activity from at least five fountain-type geysers. Fountain-type geysers erupt steam and water from open pools and in the process they accelerate large volumes of the overriding atmosphere, efficiently generating low-frequency acoustic waves. These acoustic waves are dominated by 1-8 Hz infrasound most likely because the time scales of surface accelerations occur during tenths of seconds. Corresponding wavelengths of 1-8 Hz infrasound is 40 m or longer, much larger than the vent dimension of the studied geysers. As such, sound generation may reasonably be considered as a compact, point-source volumetric signal, or a monopole. These sounds carry efficiently for hundreds of meters to several kilometers.

We did not observe any definitive infrasound signal produced by nearby cone-type geysers. Cone-type geysers are generally erupted as collimated jets of steam and water from a narrow orifice (< ~0.1 m) that is often located at the summit of a mound of sinter (or geyserite). The nearest cone-type geyser to our dual arrays was White Dome, a regular performer located only 323 m from the center of the microphone network. Although White Dome is frequently active with 9 minutes to hour-long quiescent intervals and produces a lofty jet up to 10 m it was not detected by our infrasound surveillance. Unsurprisingly, Pink Cone, another similar-sized cone-type geyser located farther away (940 m), was never definitively detected.

We speculate that cone-type geysers do not produce significant amounts of infrasound because their volumetric, or monopole, contributions are small. Instead they erupt multi-phase fluid jets, which are often modeled as dipole or quadrupole sources [**Lighthill, 1978**; **Woulff & McGetchin, 1976**; **Matoza et al., 2009**], and are much less efficient at ensonifying the atmosphere, especially in the infrasonic band. White Dome's jet is narrow and fairly low-energy. Larger cone-type geysers, such as Old Faithful and Lone Star, are more energetic and more likely to produce intense sounds. Short-duration infrasound surveys of these geysers during our August 2011 experiment indeed revealed lower infrasound spectral power and enhanced higher frequency sound, compared to fountain geysers with jets of similar height.

Our survey of the LGB confirmed that major fountain-type geysers are reliably identified with dual microphone arrays at distances of up to several kilometers. However, we note that we did not detect reliable signal from the major fountain geysers located in the UGB, located more than 8.5 km away. This suggests a limit of somewhere between 3 and 8 km for infrasound detection of major fountain-type geysers. We also note that we did not detect activity from any minor fountain type geysers farther than about 500 m distant, such as those found in the Pink Cone Group or the Black Warrior Group. Based upon our observations of the minor geyser activity at Firehole and Botryoidal Springs we conclude that to reliably track smaller features it is necessary to deploy sensors within a few hundred meters of their sources.

7.0 Conclusion

Dual acoustic arrays separated by approximately 600 m can be used to identify and track activity from individual geysers out to several kilometers. As such, future monitoring of geyser activity with non-intrusive acoustic arrays in the infrasound band is warranted. Acoustic monitoring can also complement ongoing efforts to track geyser activity, such as those measuring thermal flux in geyser outflow channels in Norris Basin [**Perry, 2000**]. Further, acoustic monitoring can facilitate comprehensive records of geyser

eruption statistics, including repose periods between eruptions, eruption duration, and style of eruption (e.g., pulsing, spasmodic or continuous, intense or benign), which will enable a better understanding of hydrologic controls including exchange of function with neighboring features [**Marler, 1951**]. Relationships between eruption duration and repose time can be also be robustly studied given continuous and long-duration monitoring of a system of geysers toward better understanding of periodicity controls [**Ingebritsen & Rojstaczer, 1993**]. Finally, we anticipate that changes in geyser activity, due to seasonal effects or dynamic strains from transient earthquake waves [**Husen et al., 2004**], can be more robustly quantified and studied with long-term acoustic monitoring.

We have shown that the ability to comprehensively monitor geysers is affected by both the intensity of the geyser infrasound source, which appears greater for fountain-type geysers than for cone-type geysers, and the level of background noise. During local daytime periods (e.g., 10:00 AM to 9:00 PM) wind was often so intense in LGB as to obscure all activity except from the nearby Great Fountain. More comprehensive monitoring of geyser activity will be facilitated with better strategic deployment of arrays closer to the smaller geothermal features and utilization of a greater number of arrays. In the future, local monitoring of the UGB with its incredible population of major geysers will be particularly illuminating. We believe that infrasound monitoring is an effective and non-intrusive tool for tracking activity for a cluster of geysers and can be substantially less work-intensive than relying upon eyewitness or video observations.

8.0 Acknowledgments

Fieldwork was carried out with help from a team of students in a volcano geophysical field methods course held in Yellowstone National Park in 2011. Students involved included the co-authors as well as A. Curtis, N. Iverson, R. Johnson, D. Krzesni, and A.Quezada-Reyes. We are indebted to GPS surveying of the sensor arrays by M. Murray. We also thank National Park Service research staff for their assistance with permitting and logistical advice. NSF EAR grant #1151662 supported this work.

9.0 References

Arechiga, R., Johnson, J.B., Edens, H., Thomas, R.J. and Rison, W., 2011. Acoustic localization of triggered lightning. J. Geophys. Res., 116(D09103).

Arrowsmith, S.J., Johnson, J.B., Drob, D.P. and Hedlin, M.A.H., 2010. The seismo-acoustic wavefield: a new paradigm in studying geophysical phenomena. Rev. Geophys., 48: RG4003.

Assink, J.D., Evers, L.G., Holleman, I. and Paulssen, H., 2008. Characterization of infrasound from lightning. Geophys. Res. Lett., 35(L15802).

Bowman, J.R., Baker, G.E. and Bahavar, M., 2005. Ambient infrasound noise. Geophysical Research Letters, 32(9).

Bryan, T.S., 2008. The geysers of Yellowstone, 4th edition. University Press of Colorado, Niwot, CO, 463 pp.

Cansi, 1995. An automatic seismic event processing for detection and location; the P.M.C.C. method. Geophys. Res. Lett., 22(9): 1021-1024.

Christie, D.R. and Campus, P., 2010. The IMS infrasound network: design and establishment of infrasound stations, Infrasonic monitoring for atmospheric studies. Springer, Heidelberg, pp. 29-75.

Dowling, A.P., 1998. Steady-state radiation from sources. In: M. Crocker (Editor), Handbook of Acoustics. John Wiley & Sons, New York, pp. 99-117.

Fee, D. and Garces, M., 2007. Infrasonic tremor in the diffraction zone. Geophys. Res. Lett. 34: L16826.

Garces, M.A. and McNutt, S.R., 1997. Theory of the airborne sound field generated in a resonant magma conduit. J. Volc. Geotherm. Res., 78(3-4): 155-178.

Gerst, A., Hort, M., Aster, R.C. and Johnson, J.B., in rev. The first second of a volcanic eruption - energies, pressures, mechanisms. J. Geophys. Res.

Husen, S., Wiemer, S. and Smith, R.B., 2004. Remotely triggered seismicity in the Yellowstone National Park region by the 2002 Mw 7.9 Denali Fault earthquake, Alaska. Bull. Seismol. Soc. Am., 94(6B): 317-331.

Ingebritsen, S.E. and Rojstaczer, S.A., 1993. Controls on geyser periodicity. Science, 262(5135): 889-892.

Johnson, J.B., Aster, R.C. and Kyle, P.R., 2004. Volcanic eruptions observed with infrasound. Geophys. Res. Lett., 31(L14604): doi:10.1029/2004GL020020.

Johnson, J.B. and Ripepe, M., 2011. Volcano infrasound: a review. J. Volc. Geotherm. Res., 206, 61-69.

Jones, K., Johnson, J.B., Aster, R., Kyle, P. and McIntosh, W., 2008. Infrasonic tracking of large bubble bursts and ash venting at Erebus volcano, Antarctica. J. Volc. Geotherm. Res., 177: 661-672.

Kedar, S., Sturtevant, B. and Kanamori, H., 1996. The origin of harmonic tremor at Old Faithful geyser. Nature, 379: 708-711.

Kieffer, S.W., 1984. Seismicity at Old Faithful Geyser; an isolated source of geothermal noise and possible analogue of volcanic seismicity. J. Volc. Geotherm. Res., 22: 59-95.

Lighthill, M.J., 1978. Waves in Fluids. Cambridge University Press, New York, 504 pp.

Marchetti, E., Ripepe, M., Harris, A.J.L. and Delle Donne, D., 2009. Tracing the differences between Vulcanian and Strombolian explosions using infrasonic and thermal radiation energy. Earth and Planetary Science Letters, 279(3-4): 273-281.

Marcillo, O., Johnson, J.B. and Hart, D., 2012. Implementation, characterization, and evaluation of an inexpensive low-power low-noise infrasound sensor based on a micro-machined differential pressure transducer and a mechanical filter. J. Atmos. Ocean. Tech. 29: 1275-1284.

Marler, G.D., 1951. Exchange of function as a cause of geyser irregularity. Am. J. Sci., 249: 329-342.

Matoza, R. et al., 2009. Infrasonic jet noise from volcanic eruptions. Geophys. Res. Lett., 36(L08303).

Murray, T.L. and Endo, E.T., 1992. A real-time seismic-amplitude measurement system (RSAM). In: Ewart and Swanson (Editors), Monitoring Volcanoes: Techniques and Strategies Used by the Staff of the Cascades Volcano Observatory, 1980-1990. USGS Bulletin, pp. 5-10.

Perry, J., 2011. Tracking Yellowstone's activity. Earth Magazine, April.

Ripepe, M. and Gordeev, E.I., 1999. Gas bubble dynamics model for shallow volcanic tremor at Stromboli. J. Geophys. Res., 104(B5): 10639-10654.

Rost, S. and Thomas, C., 2002. Array seismology: methods and applications. Rev. Geophys., 40(1008): 27 pp.

Vergniolle, S. and Brandeis, G., 1996. Strombolian explosions 1. A large bubble breaking at the surface of a lava column as a source of sound. J Geophys. Res., 101(B9): 20433-20447.

Woulff, G. and McGetchin, T.R., 1976. Acoustic noise from volcanoes: theory and experiment. Geophys. J. R. Astr. Soc., 45: 601-616.

Yokoo, A. and Iguchi, M., 2010. Using infrasound waves from eruption video to explain ground deformation preceding the eruption of Suwanosejima volcano, Japan. J. Volc. Geotherm. Res., 196(3-4): 287-294.

10.0 Table

Name	Latitude (degrees N)	Longitude (degrees W)	Elev. (m)	Dist. (m)	Interval	Duration (minutes)	Height (m)	Type
Network Center (x)	44.536614	110.801662	2231	0				
East Array (EA)	44.536765	110.797793	2238	309				
West Array (WA)	44.536462	110.805531	2229	309				
Great Fountain (GF)	44.536578	110.800026	2234	130	9-15 hours	30-120	23-67	F
Firehole Spring (FS)	44.535141	110.801949	2235	165	Continuous	Continuous	<2	F
Botryoidal Spring (BS)	44.534882	110.799529	2238	265	3-5 minutes	1	3	F
White Dome (WD)	44.539394	110.802823	2228	323	15-180 min	2	6-9	C
Pink Cone (PC/PCG)	44.542893	110.796273	2235	819	18-25 hours	90-120	< 9	C
Bead (B/PCG)	44.543418	110.794972	2239	924	27-33 min	2.5	7-8	C
Narcissus (N/PCG)	44.544322	110.797004	2235	933	2-6 hours	<15	4-6	F
Labial (B/PCG)	44.543751	110.795304	2240	940	5-7 hours	<2	<8	F
Steady (S/BWG)	44.544198	110.786705	2247	1455	Continuous	Continuous	<4	F
Artesia (A/BWG)	44.544075	110.784056	2253	1623	Continuous	Continuous	<3	F
Fountain (F/FG)	44.551205	110.808326	2228	1705	4-15 hours	30	~25	F
Kaleidescope Group (various/KG)	44.554275	110.813347	2212	~2200	Various	Various	<45	V
Middle Geyser Basin (various/MGB)	44.525055	110.838148	2218	~3200	Various	Various	<5	V
Upper Geyser Basin (various/UGB)	44.466665	110.836993	2238	~8700	Various	Various	60	V

Table 1 – Location list of microphone arrays and various geysers, geyser groups, and geyser basins near LGB: Names and abbreviations used in figures, latitude, longitude, elevation, distance from the center of the microphone network, geyser eruption repeat interval, duration of geyser activity, typical height of play, and type of geyser indicated as either (F)ountain, (C)one, or (V)arious. Details are taken from ***Bryan (2008)****.*

11.0 Figures & Captions

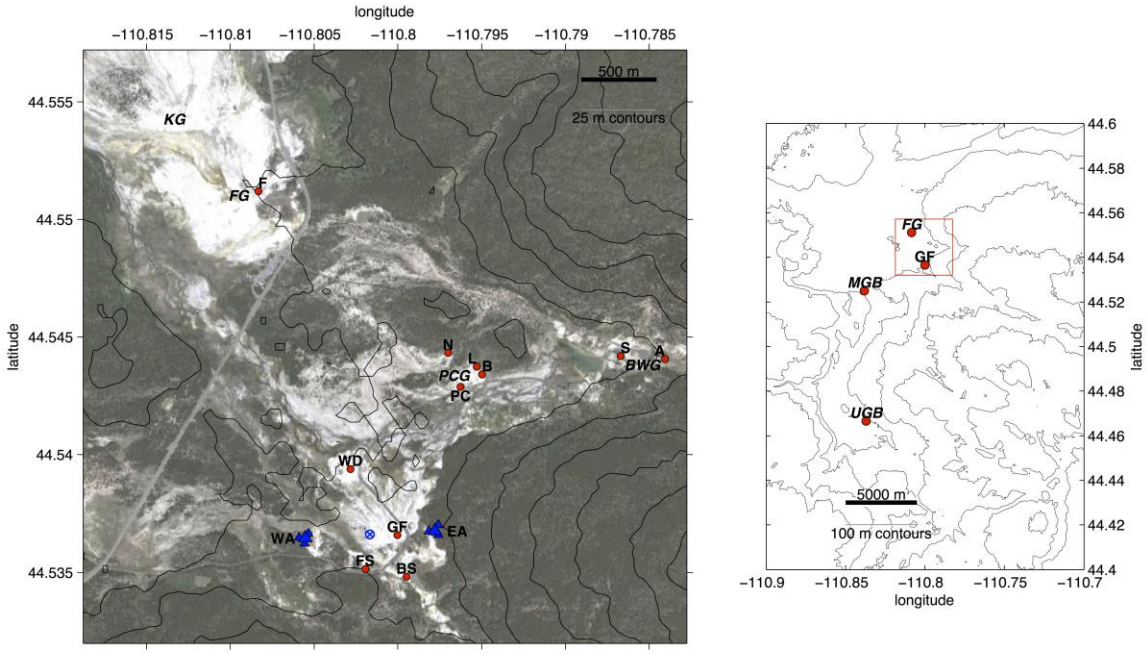

Figure 1 - Detail map featuring LGB study area. Its position relative to the Middle Geyser Basin (MGB) and Upper Geyser Basin (UGB) is given by the red rectangle in the locator map. Locations are shown for Great Fountain (GF), Firehole Spring (FS), Botryoidal Spring (BS), White Dome (WD), the Pink Cone Group (PCG) including Narcissus (N), Pink Cone (PC), Bead (B), and Labial, the Black Warrior Group (BWG) including Steady (S) and Artesia (A), the Fountain Group (FG) featuring Fountain (F), and the Kaleidescope Group (KG). Details of these geysers are summarized in Table 1. West Array (WA) and East Array (EA) microphone sites are shown as blue triangles along with the network center indicated by crosshairs. Array geometry detail is shown in Figure 2.

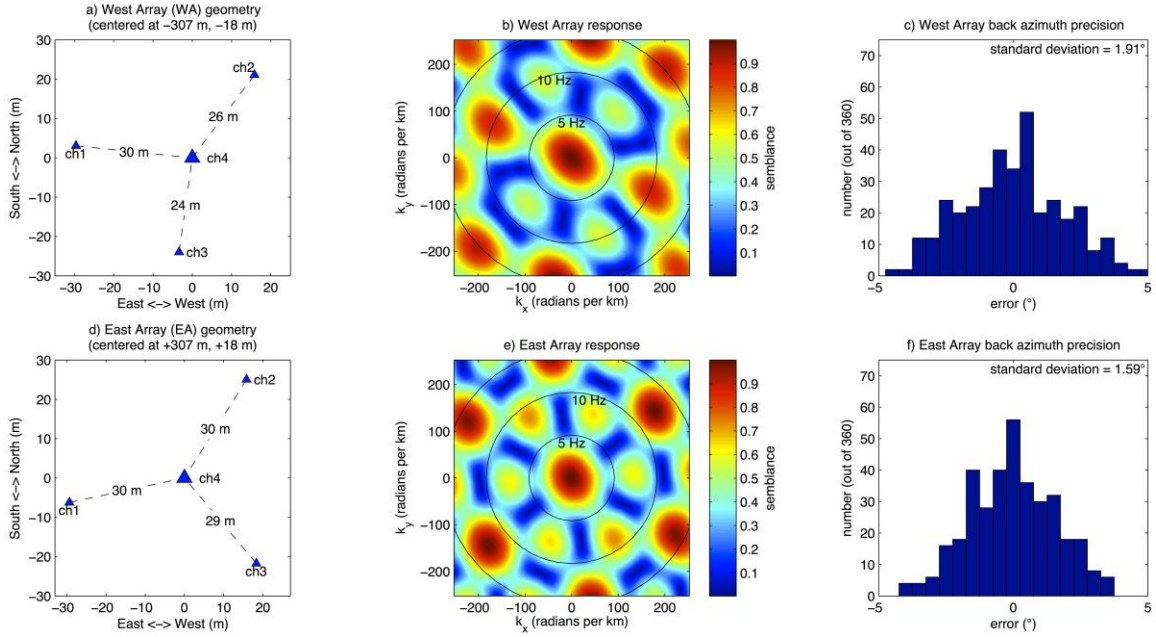

Figure 2 - a,d) Detail plan view maps of West and East microphone arrays. Parenthetical coordinates are the east-west and north-south array center location relative to the center of the network and map origin. b,e) Corresponding array responses calculated according to Eqn. 1. Contours indicate wavenumbers for 5, 10 and 15 Hz horizontal acoustic plane waves. c,f) Histograms of angular uncertainties in calculated back-azimuth for data digitally discretized to 0.01 s.

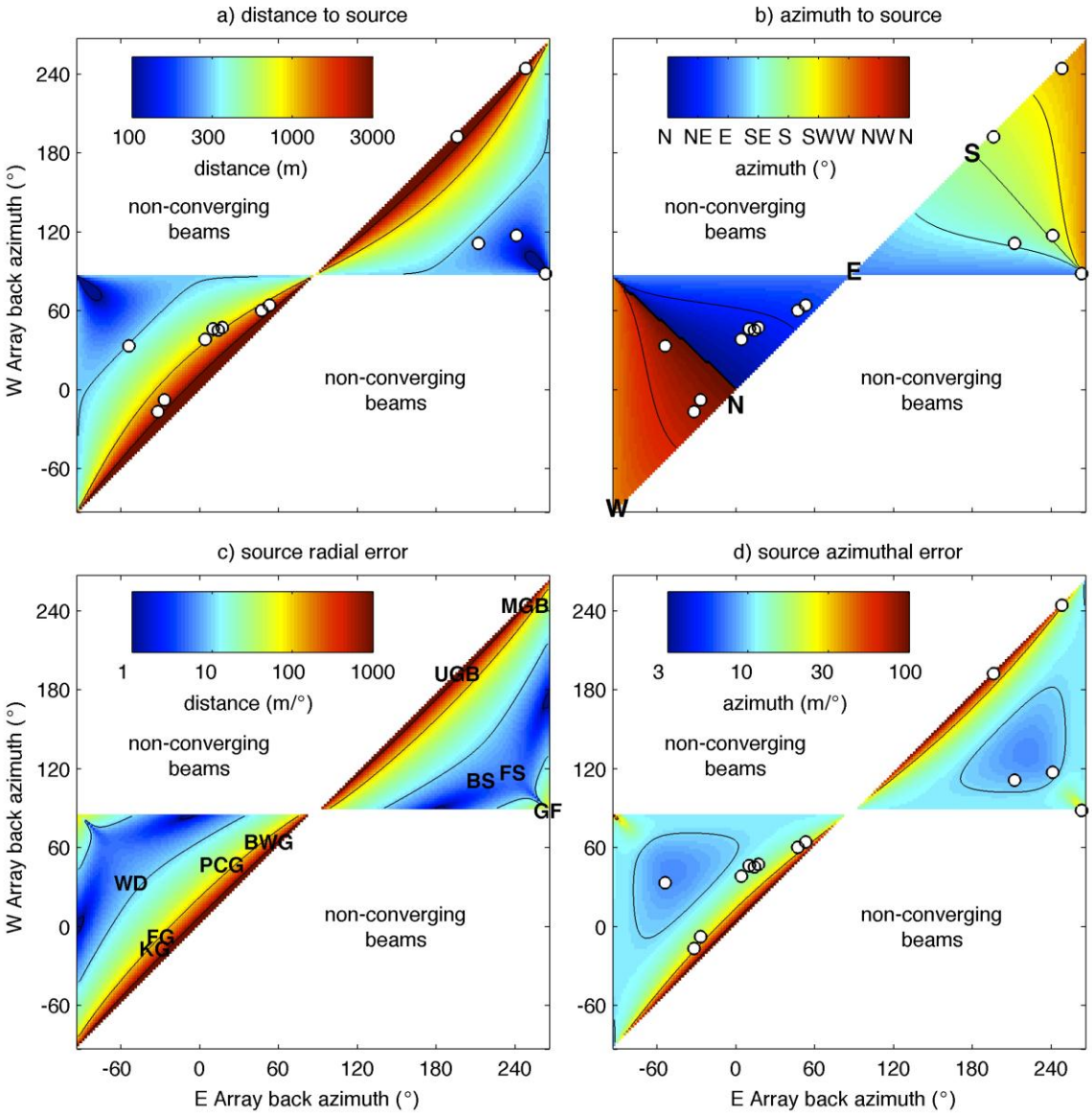

Figure 3 - a) Distance (r) to cross-beam sources for conjointly computed back-azimuths from West and East arrays. b) Compass bearing (θ) to inferred sources. c) Radial error (e_r) per degree of back-azimuth uncertainty. d) Azimuthal error (e_θ) per degree of back-azimuth uncertainty. All distance and source azimuths are relative to the network center (crosshairs in Figure 1). Blank regions correspond to non-converging back-azimuths. Expected bearing to those geysers and groups indicated in Figure 1 and Table 1 are shown as white circles with names annotated in panel c.

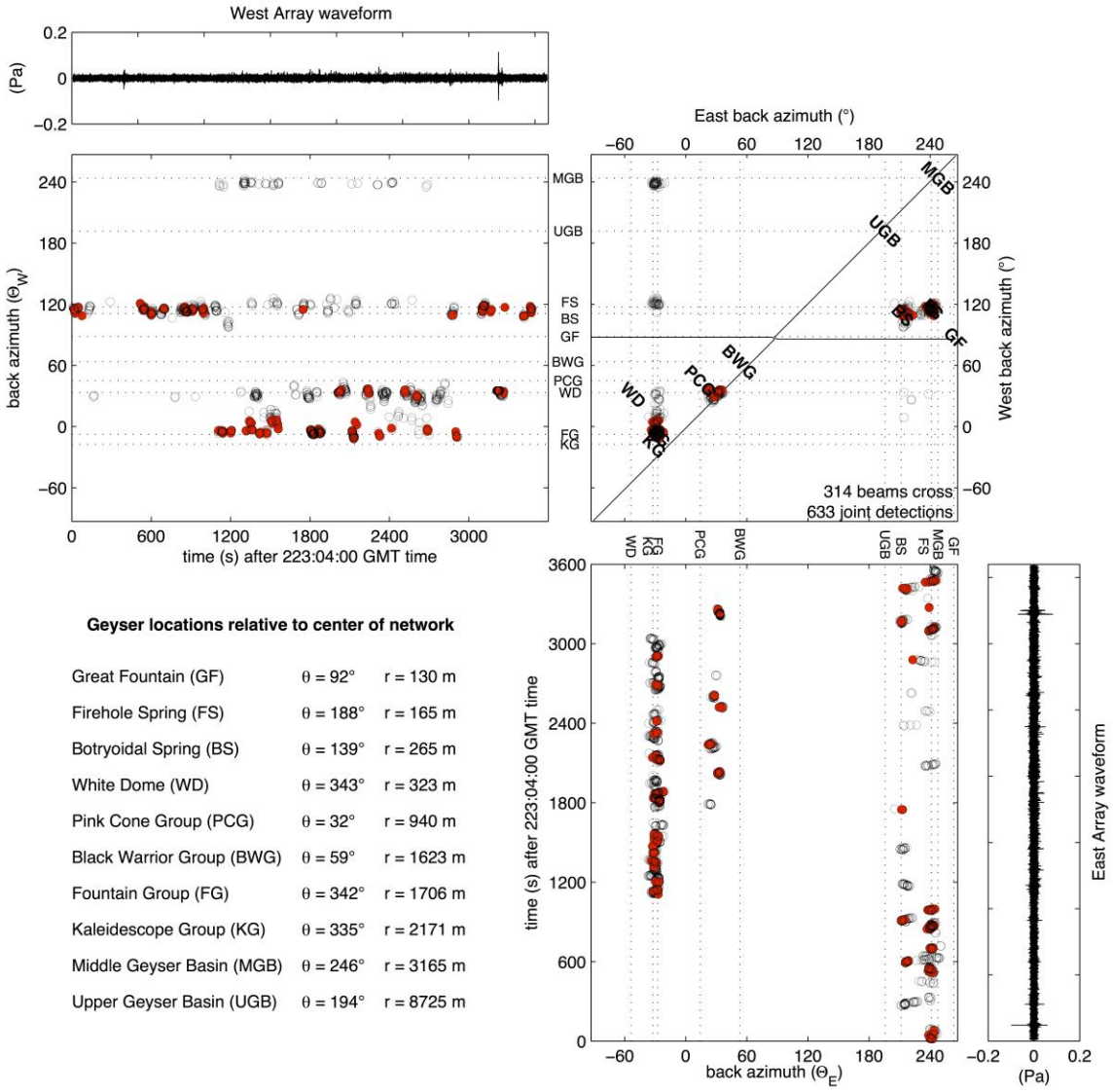

Figure 4 - (Upper left) Example 1-hour time series for West Array infrasound recording (filtered above 0.25 Hz) and calculated coherent back-azimuths for 20-s windows sliding at 1-s increments. (Lower right) corresponding time series of East Array infrasound and calculated back-azimuths. (Upper right) map of conjoint back-azimuths from the two arrays. Red-filled symbols indicates conjoint sources with associated converging back-azimuths. Back-azimuths for various geyser basins, geyser groups, or specific geysers that are indicated in Figure 1 and Table 1 are shown and described in lower left text panel. Data shown are from a one-hour period starting August 10th at 10:00 PM local time (Julian Day 223 at 04:00). Corresponding detection source locations and example waveforms for this hour are shown in Figures 5 and 6.

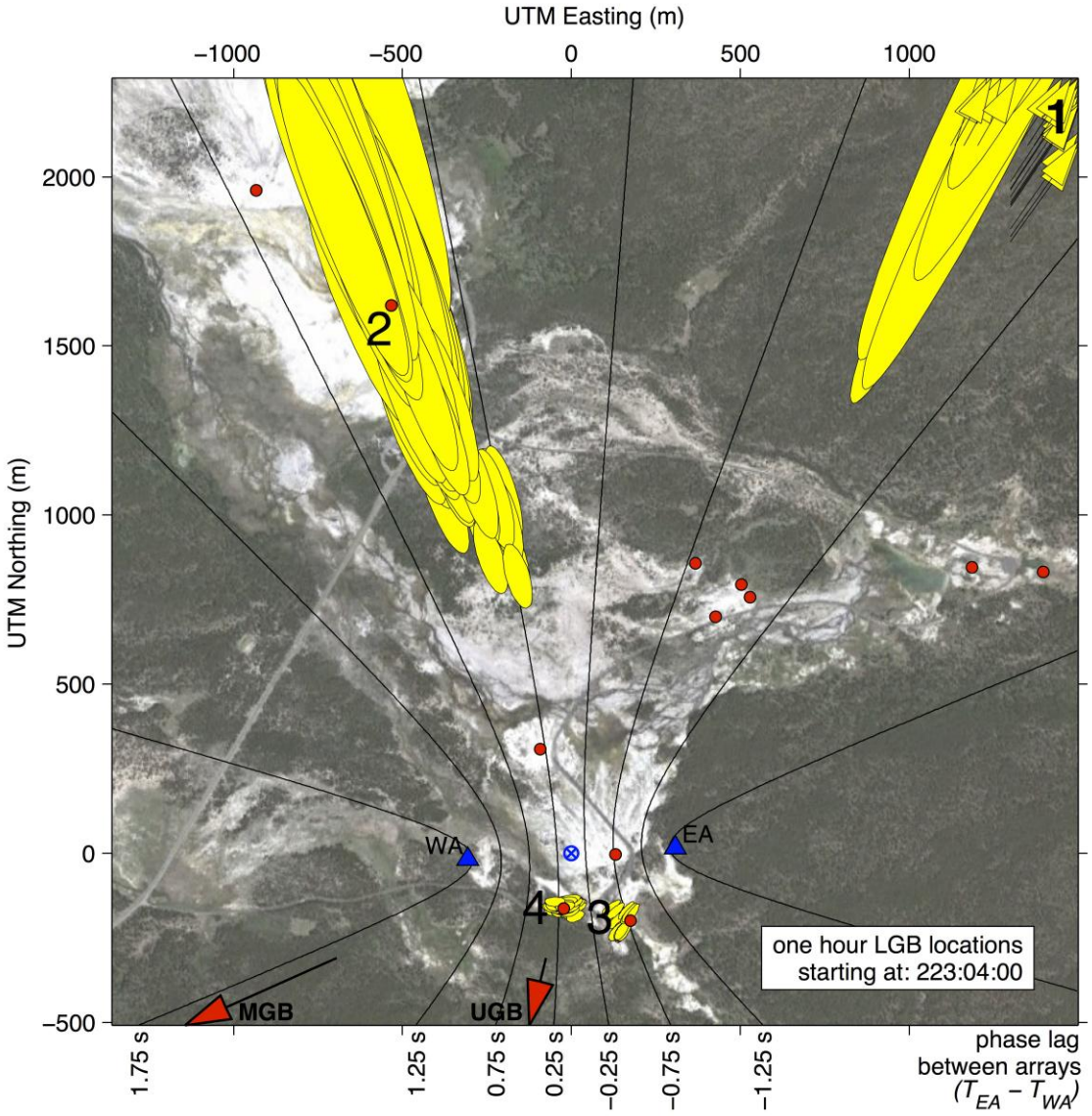

Figure 5 - Map of infrasound sources occurring during the-one hour period shown in Figure 4. Locations of candidate geysers (from Table 1 and Figure 1) are marked by red circles while red arrows indicate direction to geyser basins located off the map. Map origin, indicated by crosshair, is the center of the two arrays indicated by blue triangles. Contours indicate expected time lag delays between the East Array and West Array. Ellipses designate those conjoint back-azimuth intersections, which have been validated by inter-network lag time delays and for which incidence is nearly horizontal (i.e., elevation angles less than 15°). Sources located off map are indicated with yellow arrows. Numbered source epicenters correspond to featured events shown in Figure 6. Events #2-4 correspond to geyser activity.

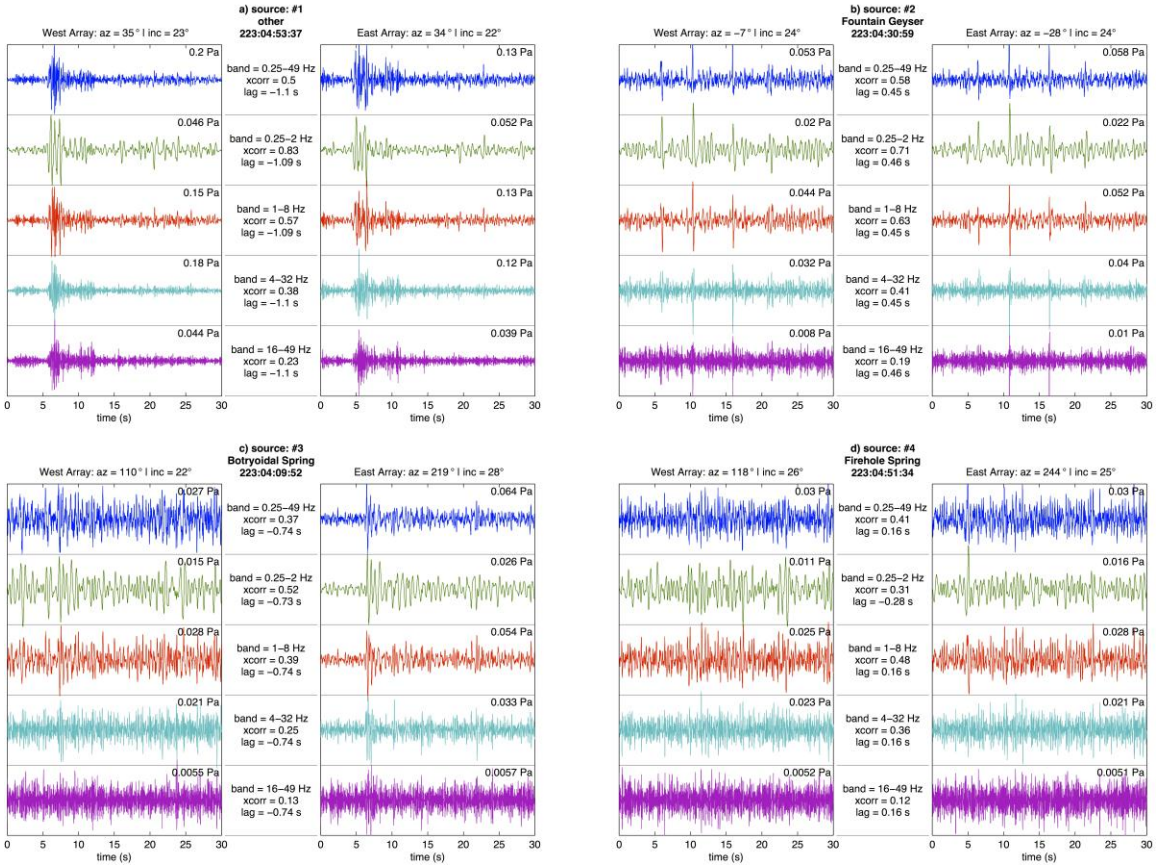

Figure 6 - Detail beam stack waveforms filtered into five frequency bands using 2-pole Butterworth filters with the indicated corner frequencies. Peak-to-peak signal amplitudes, normalized correlation coefficients, and associated peak correlation lag times are shown for each waveform and each band. Featured events correspond to the best correlated signals occurring in Figure 4 from four representative source regions including: a) probable distant thunder source(s) to the Northeast of the LGB, b) Fountain Geyser ~1700 m, c) Botryoidal Spring ~250 m, and d) Firehole Spring ~150 m from the network center.

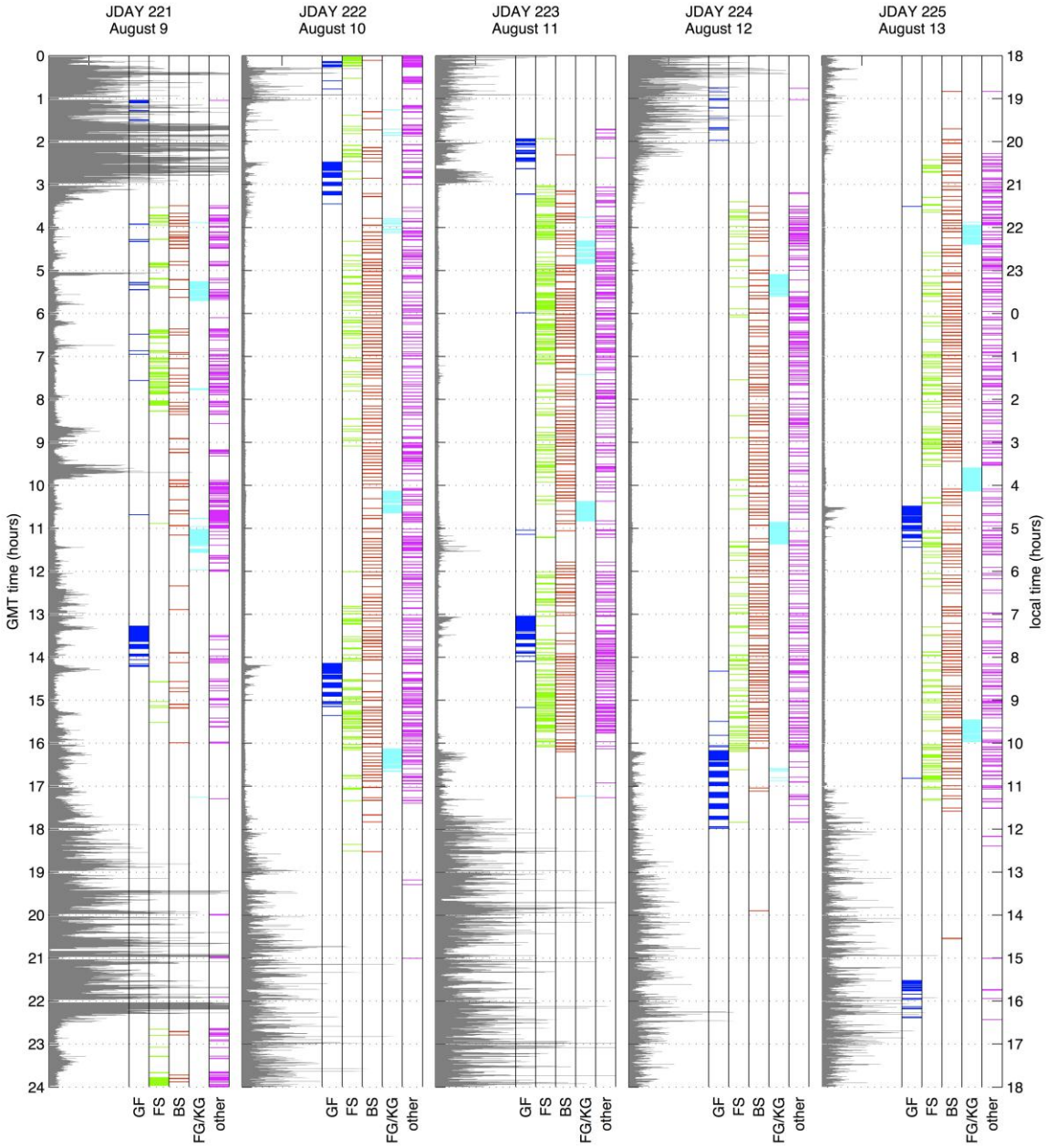

*Figure 7 - Infrasound detections from a 5-day interval in August 2011. Featured geysers and their detected activity include Great Fountain (GF; blue), Firehole Spring (FS; green), Botyroidal Spring (BS; red), Fountain and Kaleidescope (FG/KG; cyan), and other sources (other; mauve). Each detection corresponds to coherent energy identified on the EA. Grey records correspond to 20-s averaged absolute signal amplitudes, analogous to real-time seismic amplitude measurements [**Murray & Endo, 1992**].*

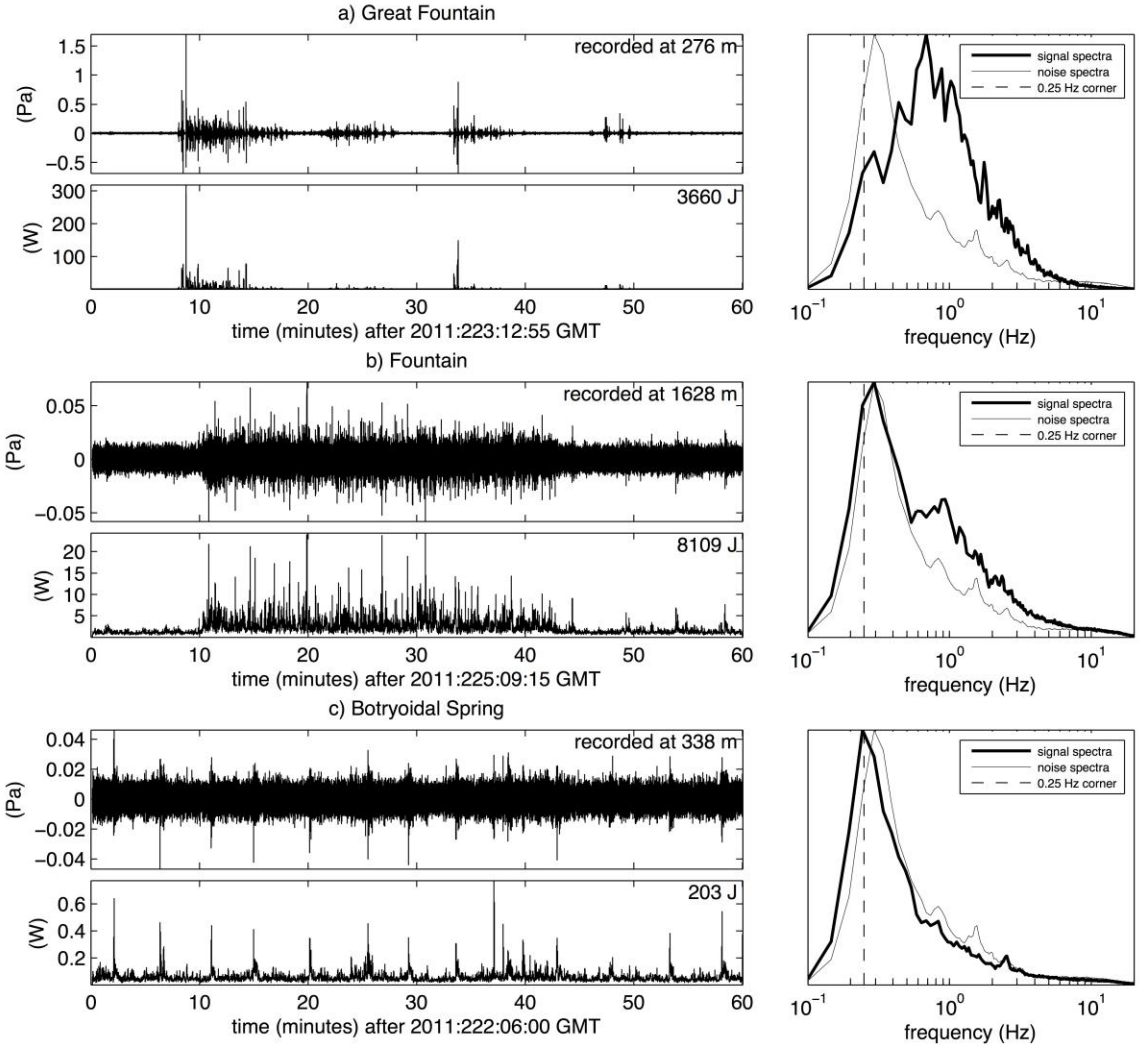

Figure 8 - One-hour pressure time series, acoustic power, and corresponding power spectral density for select events at: a) Great Fountain, b) Fountain Geyser, and c) Botryoidal Spring. Data are shown for band-pass filtered (0.25-20 Hz) signal. Acoustic power is calculated according to Eqn. 11 using Δt =1 s intervals. Total energy for the hour-long interval is shown in each panel. Power spectral density shows a combination of ambient infrasonic noise, centered at the 0.25 Hz corner frequency (dashed line), as well as generally higher frequency geyser signal. Power spectrum from a low-noise one-hour nighttime period is indicated for comparison.

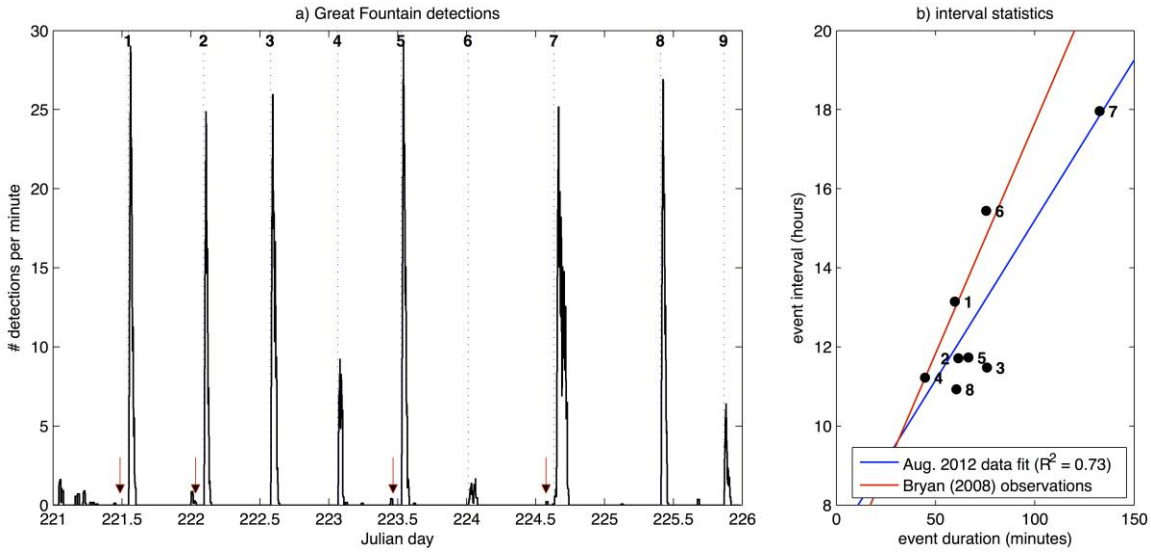

Figure 9 – a) Five-day record of Great Fountain event detections showing episodicity of events. Red arrows are drawn 85 minutes prior to select main events and coincide with some detected precursors. b) Duration of event detections plotted against subsequent quiescent interval for 8 events (black circles). Event interval is measured as the time between a main event's last detection and the next event's first detection.

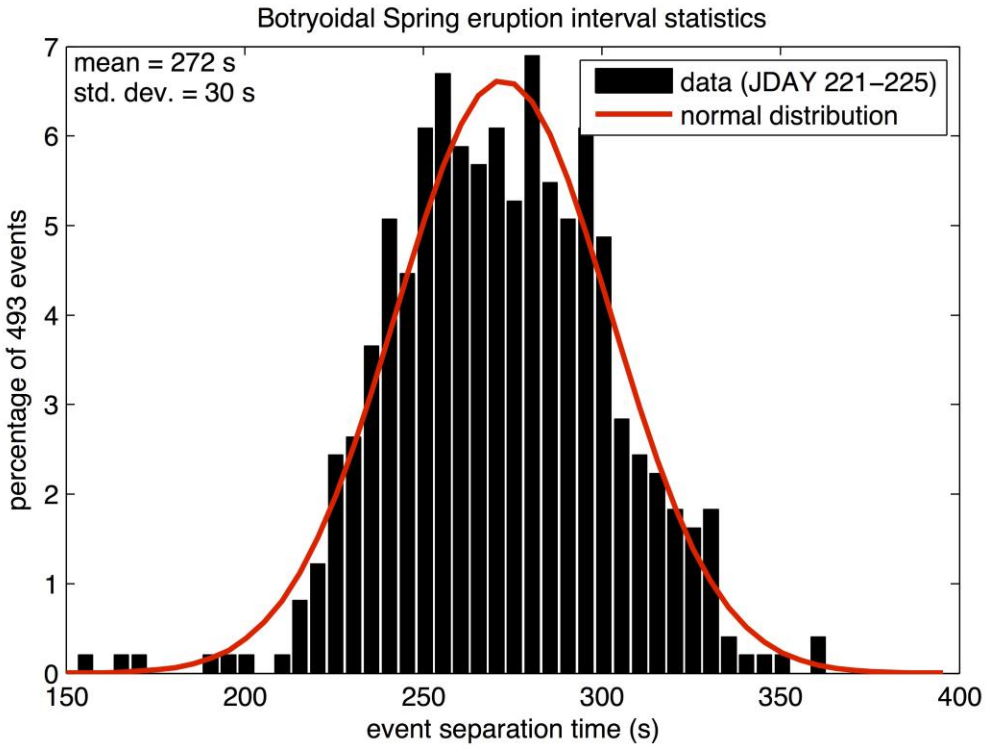

Figure 10 – Distribution of event intervals for detected Botryoidal Spring eruptions. Intervals are defined as time differences between center times of successive event detections. Normal distribution fit to data is shown.